

Nonparaxial corrections for short cavities and fibers

E. S. Hissink, C. Koks , and M. P. van Exter 

Huygens-Kamerlingh Onnes Laboratory, Leiden University, PO Box 9504, 2300 RA Leiden, The Netherlands



(Received 17 August 2022; accepted 26 October 2022; published 7 November 2022)

This paper describes optical propagation beyond the paraxial limit in rotational symmetric short Fabry-Pérot cavities and long fibers with parabolic-index profiles. Frequency shifts due to paraxial and nonparaxial effects, the so-called spectral fine structure and vector corrections, are calculated with perturbation theory and expressed in a single dimensionless expansion parameter. The results obtained for short cavities and fibers have similar functional forms but are surprisingly different. These similarities and differences are pointed out and discussed, including their consequences for mode multiplexing in fibers.

DOI: [10.1103/PhysRevA.106.053505](https://doi.org/10.1103/PhysRevA.106.053505)

I. INTRODUCTION

Rotational symmetric Fabry-Pérot (FP) microcavities are well-known tools in optics. They are among others used as a spectrum analyzer and as a means to trap light [1,2]. The paraxial description of these cavities predicts that their resonance spectra, observed upon scanning either optical frequency or cavity length, consist of a series of equidistant peaks [3]. This prediction works reasonably well for macroscopic cavities but breaks down when the optical modes are compact and hence have large opening angles. A proper description of such resonances requires the inclusion of several nonparaxial corrections.

Nonparaxial corrections to the propagation of light have been a popular topic of research since the 1970s [4,5]. But nonparaxial corrections to the boundary conditions are equally important for cavities. The first complete description of the fine structure in FP spectra, including nonparaxial propagation and reflection corrections, was formulated in the 1980s [6–8] and reformulated in 2010 [9]. This nonparaxial theory was recently extended in a paper on the fine structure of microcavity Fabry-Pérot spectra [10], and several predictions therein were experimentally confirmed [11]. We will use these recent and more complete publications as our main references.

In this paper, we will apply the nonparaxial theory from Ref. [10] to the common geometry of short FP cavities, where “short” means that the cavity length is much smaller than the radius of curvature of the spherical mirror. In this short-cavity limit, the focusing and defocusing effects of propagation and reflection can be spread uniformly over the cavity, such that the “unfolded” cavity resembles an optical transmission line or fiber. In Sec. II, we show that these effects are then described by a single parameter: the paraxial Rayleigh range z_0 . The resulting expressions are surprisingly elegant and clearly show the origin of various nonparaxial corrections.

Section III describes the nonparaxial propagation of light in fibers with an infinite parabolic refractive-index profile, which is a common approximation for multimode graded-index fibers. It includes the so-called vector correction, which results in spin-orbit coupling [12,13], but also introduces a

new (scalar) nonparaxial correction. This description is important because spatial mode multiplexing as a tool to increase the bandwidth in fiber communication [14–19] works only if these spatial modes are sufficiently different to act as independent channels, i.e., if their modal refractive indices are sufficiently different. The nonparaxial corrections discussed in this paper are essential to create these differences. Section IV compares the nonparaxial corrections in cavities and fibers. Section V concludes with a summary and outlook.

II. NONPARAXIAL FINE STRUCTURE FOR SHORT CAVITIES

Consider a stable Fabry-Pérot cavity in vacuum with a planar mirror at $z = 0$ and a concave spherical mirror with curvature radius R_m at $z = L$. Both mirrors are assumed to be ideal, the cavity is perfectly rotationally symmetric, and losses are neglected.

The intracavity field \vec{E} should satisfy the wave equation $(\Delta + k^2)\vec{E} = 0$ and the boundary conditions at the mirrors. The paraxial solutions of this problem are well known [3]. They can be derived by writing the forward-propagating component of the scalar optical field as $E(r, \theta, z) = \psi(r, \theta, z) \exp(ikz)$ and by approximating the exact rewrite on the left with the paraxial result on the right [3]:

$$\left(2ik \frac{\partial}{\partial z} + \Delta_{\perp} + \frac{\partial^2}{\partial z^2}\right)\psi = 0 \Rightarrow \left(2ik \frac{\partial}{\partial z} + \Delta_{\perp}\right)\psi \simeq 0, \quad (1)$$

where $\Delta_{\perp} = \partial^2/\partial x^2 + \partial^2/\partial y^2$. The paraxial wave equation on the right has a series of exact solutions in the form of Laguerre-Gaussian (LG) modes [10,20]:

$$\begin{aligned} \psi_{p,\ell}(r, \theta, z) &= \frac{1}{\gamma(z)} \Psi_{p,\ell}(\tilde{r}, \theta, \chi) e^{i \frac{kz^2}{2R(z)}} \\ &= \frac{\cos \chi}{\gamma_0} \Psi_{p,\ell}(\tilde{r}, \theta, \chi) e^{i \tan \chi \frac{r^2}{2}}, \quad (2) \\ \Psi_{p,\ell}(\tilde{r}, \theta, \chi) &= \Phi_{p,\ell}(\tilde{r}, \theta) e^{-i(N+1)\chi} \\ &= f_{p,\ell}(\tilde{r}) e^{i\ell\theta} e^{-i(N+1)\chi}. \quad (3) \end{aligned}$$

Equation (2) expresses the LG modes in terms of normalized LG modes with normalized radial position $\tilde{r} \equiv r/\gamma(z)$ by removing the wave-front curvature and the transverse scaling by introducing the beam width $\gamma(z) = \gamma_0 \sqrt{1 + (z/z_0)^2} = \gamma_0/\cos\chi$, the fundamental Gouy phase $\chi = \chi(z) = \arctan(z/z_0)$, and the radius of curvature $R(z) = (z^2 + z_0^2)/z = 2z_0/\sin(2\chi)$. The wave fronts of these solutions match the shape of the flat mirror at $z = 0$ and the radius of curvature of the concave mirror when $R(L) = R_m$, i.e., when $z_0 = k\gamma_0^2 = \sqrt{L(R_m - L)}$ with wave vector $k = 2\pi/\lambda$ and wavelength λ . Equation (3) removes the (Gouy-phase-induced) longitudinal phase slip. It also introduces the normalized radial function $f_{p,\ell}(\tilde{r}) \propto \tilde{r}^\ell \mathcal{L}_p^\ell(\tilde{r}^2) \exp(-\tilde{r}^2/2)$, with the generalized Laguerre polynomial $\mathcal{L}_p^\ell(\tilde{r}^2)$, and the orbital angular momentum (OAM) phase factor [10,21]. The radial mode number p and OAM number $\tilde{\ell} = \pm\ell$ together determine the transverse order $N = 2p + \ell$. The $\tilde{\ell} = \ell$ and $-\ell$ solutions are simple mirror images with identical resonance frequencies in a mirror-symmetric system.

Equation (2) applies to all solutions $\psi_{p,\tilde{\ell}}$ and can thus also be interpreted as a coordinate transformation from the actual position (r, z) to the normalized dimensionless position (\tilde{r}, χ) . This change in coordinates, which involves a Jacobian with an off-diagonal element $\partial\tilde{r}/\partial z \neq 0$, modifies the right-hand side of Eq. (1) to the normalized paraxial equation [20–22]

$$i \frac{\partial}{\partial \chi} \Psi = \left(-\frac{1}{2} \tilde{\Delta}_\perp + \frac{1}{2} \tilde{r}^2 \right) \Psi \equiv \tilde{\mathcal{H}}_{\text{par}} \Psi, \quad (4)$$

where the tildes indicate dimensionless forms and where $\tilde{\Delta}_\perp = \gamma(z)^2 \Delta_\perp$ and $\tilde{r} = r/\gamma(z)$. Equation (4) shows that the evolution of the field profile in normalized coordinates is identical to the evolution of the wave function of the two-dimensional harmonic oscillator in quantum mechanics, where the Gouy phase χ acts as a time coordinate [20–22]. The two systems have identical eigenmodes $\Psi_{p,\tilde{\ell}}$, as described by Eq. (3), and identical eigenvalues $(N + 1)$.

In the short-cavity limit $L \ll R_m$, where $\chi \simeq z/z_0 \equiv \tilde{z} \ll 1$ and $\gamma(z) \simeq \gamma_0$, Eq. (4) can be written as

$$i \frac{\partial}{\partial z} \Psi \simeq \frac{\tilde{\mathcal{H}}_{\text{par}}}{z_0} \Psi = \left(-\frac{1}{2k} \Delta_\perp + \frac{kr^2}{2LR_m} \right) \Psi. \quad (5)$$

This equation has an appealing physical interpretation when we interpret the partial derivative $\partial/\partial z$ as the spread-out, coarse-grained evolution of the field over multiple round trips in the unfolded cavity (see Fig. 1). Each reflection from the concave mirror will then approximately imprint a phase factor $\exp(-2ikz_m) = \exp(-ikr^2/R_m) \simeq 1 - ikr^2/R_m$ on the wave, where $z_m = r^2/2R_m > 0$ is the quadratic part of the mirror shape. If we spread this phase change over the round-trip length $2L$, we recover the $kr^2/(2LR_m)$ potential in Eq. (5) and conclude that this potential originates from the spherical mirror shape. For completeness, we note that the same result can be derived by applying the effective-index model of Hadley [23] to a short Fabry-Pérot cavity [24]. This model, which is valid if the effective potential varies sufficiently slowly over the beam profile, states that optical propagation in the unfolded cavity resembles optical propagation in a fiber with an effective-index profile $n_{\text{eff}}^2(r) = 1 - (r/z_0)^2$, where

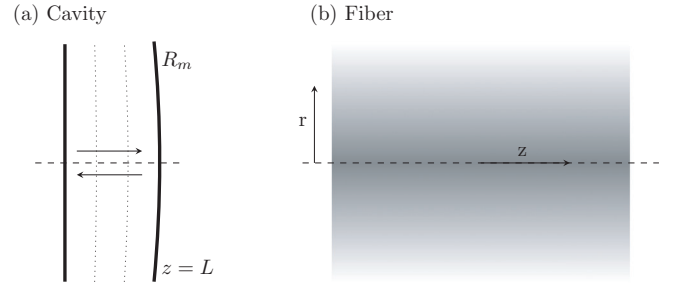


FIG. 1. Sketches of the considered geometries: (a) Short cavity with a planar mirror and a curved mirror with the radius of curvature R_m at a distance $L \ll R_m$. (b) Fiber with parabolic profile $n^2(r)$. The to-and-fro paths between the mirrors in (a) can be unfolded into a one-way propagation like that in the fiber in (b).

$z_0 = \sqrt{LR_m}$; the case with core index $n_{\text{core}} \neq 1$ follows from scaling.

Next, we introduce nonparaxial corrections by replacing $\tilde{\mathcal{H}}_{\text{par}}$ in Eqs. (4) and (5) by $\tilde{\mathcal{H}}_{\text{par}} + \tilde{\mathcal{H}}_{\text{fine}}/(kz_0)$. This replacement is inspired by the analysis in Ref. [10], where the evolution per round trip is described by a round-trip operator M that transforms the field profile Ψ into $M\Psi = \exp[i(2kL - \mathcal{H})]\Psi$ after one round trip with $\mathcal{H} = \mathcal{H}_{\text{par}} + \mathcal{H}_{\text{fine}}$. Our operator $\tilde{\mathcal{H}}_{\text{par}} = [z_0/(2L)]\mathcal{H}_{\text{par}}$ because $\tilde{\mathcal{H}}_{\text{par}}$ describes the change per Rayleigh range z_0 , whereas \mathcal{H}_{par} in Ref. [10] describes the change per round trip $\Delta z = 2L$. And our operator $\tilde{\mathcal{H}}_{\text{fine}} = [kz_0^2/(2L)]\mathcal{H}_{\text{fine}}$ includes an additional factor kz_0 because we chose to remove the expansion parameter $\alpha = 1/(kz_0)$ from the strengths of all nonparaxial effects.

The nonparaxial operator contains several scalar and vector contributions, described by $\tilde{\mathcal{H}}_{\text{fine}} = \tilde{\mathcal{H}}_{\text{scalar}} + \tilde{\mathcal{H}}_{\text{vec}}$. The nonparaxial evolution of the scalar field is described by

$$iz_0 \frac{\partial}{\partial z} \Psi = \left(\tilde{\mathcal{H}}_{\text{par}} + \frac{1}{kz_0} \tilde{\mathcal{H}}_{\text{scalar}} \right) \Psi. \quad (6)$$

Following Ref. [10], we split $\tilde{\mathcal{H}}_{\text{scalar}}$ into a propagation correction $\tilde{\mathcal{H}}_{\text{prop}}$ and a wave-front or reflection correction $\tilde{\mathcal{H}}_{\text{wave}}$. We further split $\tilde{\mathcal{H}}_{\text{wave}}$ into a correction $\tilde{\mathcal{H}}_{\text{curv}}$ that acts via the wave-front curvature $1/R(z)$ and a correction $\tilde{\mathcal{H}}_{\text{Gouy}}$ that acts via the Gouy phase $\chi(z)$. Appendix A discusses the origin of these effects and shows that

$$\begin{aligned} \tilde{\mathcal{H}}_{\text{scalar}} &= \tilde{\mathcal{H}}_{\text{prop}} + \tilde{\mathcal{H}}_{\text{curv}} + \tilde{\mathcal{H}}_{\text{Gouy}} \\ &= \frac{1}{8} \left(\tilde{\Delta}_\perp^2 + 2\tilde{r}^4 - 4i\tilde{r}^2 \frac{\partial}{\partial \tilde{z}} \right) \end{aligned} \quad (7)$$

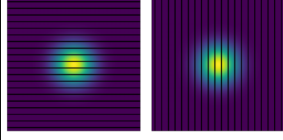
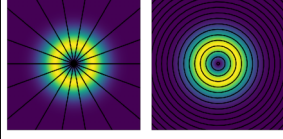
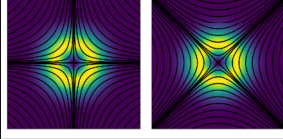
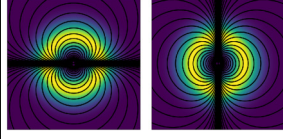
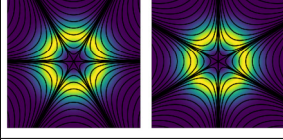
in the short-cavity limit of a more general theory [10].

Next, we consider the nonparaxial vector correction $\tilde{\mathcal{H}}_{\text{vec}}$, which results from the polarization character of the field. We now write the transverse field as a two-component vector $\tilde{\Psi}_\perp$ and express its evolution as

$$iz_0 \frac{\partial}{\partial z} \tilde{\Psi}_\perp = \left(\tilde{\mathcal{H}}_{\text{par}} + \frac{1}{kz_0} \tilde{\mathcal{H}}_{\text{scalar}} + \frac{1}{kz_0} \tilde{\mathcal{H}}_{\text{vec}} \right) \tilde{\Psi}_\perp, \quad (8)$$

where $\tilde{\mathcal{H}}_{\text{vec}}$ is a 2×2 matrix operator acting on $\tilde{\Psi}_\perp$. The vector correction originates from the unavoidable and typically weak longitudinal component of the optical field, which

TABLE I. Quantum numbers, mode profiles (intensity in false color, polarization shown by black lines), and labels or names of all vector-LG modes. The $\ell = 0$ modes come in pairs. The $\ell \geq 1$ modes come in double pairs. The two modes within each pair are rotated over an angle $\pi/(2m)$ with respect to each other, except for the $J = 0, \ell = 1$ modes, which have a uniform radial or azimuthal polarization. The labeling of cavity modes contains the absolute OAM ℓ , the A or B spin-orbit alignment, and the $+$ or $-$ mirror symmetry in the x axis. It does not contain the radial quantum number p and instead uses the group number $N = 2p + \ell$. The corresponding labeling of fiber modes starts with the spin-orbit alignment (HE, EH, TM, or TE) and contains the absolute total OAM J and $m = p + 1$. It does not contain the mirror symmetry, except for the special $J = 0$ TM/TE modes.

Quantum numbers	Mode profile	Mode label cavity	Mode label fiber
$\ell = 0, J = 0$		$0+ = X$ $0- = Y$	HE _{1m}
$\ell = 1, J = 0$		$1A+$ $1A-$	TM _{0m} TE _{0m}
$\ell = 1, J = 2$		$1B+$ $1B-$	HE _{2m}
$\ell = 2, J = 1$		$2A+$ $2A-$	EH _{1m}
$\ell = 2, J = 3$		$2B+$ $2B-$	HE _{3m}
$\ell \geq 2, J = \ell - 1$		$\ell A+$ $\ell A-$	EH _{Jm}
$\ell \geq 2, J = \ell + 1$		$\ell B+$ $\ell B-$	HE _{Jm}

generates an extra transverse field upon reflection. The associated vector operator $\mathcal{H}_{\text{vec}} = [2/(kR_m)]\vec{r}_\perp \otimes \vec{\nabla}_\perp$ in the notation used in [10], which corresponds to

$$\tilde{\mathcal{H}}_{\text{vec}} = \tilde{\vec{r}}_\perp \otimes \tilde{\vec{\nabla}}_\perp = -\frac{1}{2}(I_2 + \sigma_z \hat{\Sigma}_3), \quad \sigma_z = \begin{pmatrix} 1 & 0 \\ 0 & -1 \end{pmatrix}, \quad (9)$$

in normalized coordinates. The final equation expresses the operator in the basis of the circularly polarized unit vectors $\hat{e}_\pm = (\hat{e}_x \pm i\hat{e}_y)/\sqrt{2}$ and introduces the Pauli spin matrix σ_z and the Stokes operator $\hat{\Sigma}_3 = \hat{n}_+ - \hat{n}_-$. The combination $\sigma_z \hat{\Sigma}_3$ corresponds to a spin-orbit coupling, with $\sigma_z \hat{\Sigma}_3 = s\tilde{\ell}$ for the vector eigenmodes with $(s) = \pm 1$ and $(n_+ - n_-) = \tilde{\ell}$. The paraxial circularly polarized eigenmodes are $\tilde{\Psi}_\perp(r, \theta, z) = \exp[-i(N+1)\chi]\tilde{\Phi}_\perp(r, \theta)$, where

$$\tilde{\Phi}_\perp(r, \theta) = f(r)e^{i\tilde{\ell}\theta}\tilde{e}_\pm = f(r)e^{i\tilde{\ell}\theta}(\tilde{e}_r \pm i\tilde{e}_\theta)/\sqrt{2}, \quad (10)$$

with $\tilde{J} = \tilde{\ell} \pm 1$ and $(\tilde{e}_\pm, \tilde{e}_r, \tilde{e}_\theta)$ being unit vectors in the circular, radial, and azimuthal directions, respectively. The associated eigenvalues are (see Appendix B)

$$\langle \tilde{\Psi}_\perp | \tilde{\mathcal{H}}_{\text{vec}} | \tilde{\Psi}_\perp \rangle = \mp \tilde{J}/2 = -(1 + \tilde{\ell}s)/2. \quad (11)$$

The eigenmodes described by Eq. (10) come in different flavors. Table I summarizes the labeling of the associated vector-LG modes, which are superpositions of circularly polarized vector modes and their mirror images. Table I also shows the intensity and spatially varying linear polarization patterns of these modes for $p = 0$; the $p \geq 1$ modes have more intensity rings with identical polarization patterns. For $\ell = 0$ the mentioned superposition results in modes with a uniform x or y polarization, which we call the $0X$ and $0Y$ mode or the $0+$ and $0-$ mode, where the $+$ or $-$ label refers to their symmetry under reflection around the x axis. For $\ell \geq 1$, the four eigenmodes with $\tilde{\ell} = \pm\ell$ and $s = \pm 1$ come in two flavors, depending on the alignment of the OAM and the spin angular momentum (SAM). The (parallel) B modes have total angular momentum $\tilde{J} = \tilde{\ell} + s = \pm J$, with $J = \ell + 1$ [7,10]. The (antiparallel) A modes also have $\tilde{J} = \pm J$, but now with $J = |\ell - 1|$. Spin-orbit coupling lifts the frequency degeneracy of the A and B modes but does not remove the twofold degeneracy between the $+$ and $-$ modes. Hence, for each set of quantum numbers ($p, \ell \geq 1$) we expect two pairs of modes: the $(\ell A+, \ell A-)$ modes and the $(\ell B+, \ell B-)$ modes. In systems with imperfect rotation symmetry the frequency

degeneracy between the $\ell = 0$ linearly polarized modes is slightly lifted by shape birefringence [10,25]. The frequency degeneracy within the A and B mode pairs can then also be slightly lifted, in particular for the $1A$ modes, which have $\tilde{J} = 0$ and have either radial or azimuthal polarization. We refer to Appendix D of Ref. [10] for a more extensive discussion of these so-called hyperfine splittings.

The nonparaxial operators in Eq. (8) can potentially couple different paraxial modes. However, this mode coupling

typically goes unnoticed because light coupled to modes with different transverse orders N is typically detuned from the cavity resonance and hence does not interfere constructively [10]. As the considered nonparaxial operators are diagonal in the subset of vector-LG modes of order N , they affect only their modal wave vector $k_z = k + \delta k_j$, with $\delta k_j < 0$, $\Psi_j(z) = \exp(i\delta k_j z)\Psi_j(0)$, and $i\partial\Psi_j/\partial z = -\delta k_j\Psi_j$. After some calculation we thus find the key result [10,11],

$$\begin{aligned} \frac{\delta k_j}{k} &= -\frac{1}{kz_0} \iint \tilde{\Psi}_j^\dagger \left[\tilde{\mathcal{H}}_{\text{par}} + \frac{\tilde{\mathcal{H}}_{\text{Gouy}} + \tilde{\mathcal{H}}_{\text{curv}} + \tilde{\mathcal{H}}_{\text{prop}} + \tilde{\mathcal{H}}_{\text{vec}}}{kz_0} \right] \tilde{\Psi}_j dx dy \\ &= -\frac{N+1}{kz_0} - \frac{1}{2(kz_0)^2} \left[-(N+1)^2 + \frac{3}{4}f(N, \ell) - (1 + \tilde{\ell}_s) \right], \end{aligned} \quad (12)$$

where $f(N, \ell) = \langle \tilde{\Delta}_\perp^2 \rangle = \langle \tilde{r}^4 \rangle = \frac{3}{2}(N+1)^2 - \frac{1}{2}(\ell^2 - 1)$.

This final result highlights the $1/(kz_0)$ and $1/(kz_0)^2$ scaling of the paraxial and nonparaxial contributions. The paraxial and nonparaxial contributions scale with the square and fourth power of the opening angle Θ_0 of the fundamental mode since $\alpha = 1/(kz_0) = 1/(k\gamma_0)^2 = \Theta_0^2$, where γ_0 and Θ_0 are both radii at $1/e$ of the maximum intensity.

The final result also shows the origin of the three nonparaxial contributions: (i) the $(N+1)^2$ term originates from the wave-front correction associated with the Gouy phase, (ii) the $f(N, \ell)$ term originates from the combination of a nonparaxial propagation correction k_\perp^4 and a nonparaxial r^4 correction to the curvature of the wave front, and (iii) the $(1 + \tilde{\ell}_s)$ term originates from the vector correction upon reflection.

Equation (12) agrees with the results obtained in Refs. [10,11], with minor differences. First, it expresses the relative modal shift as $\delta k_j/k$, whereas Refs. [10,11] used $\Delta\tilde{\nu} = \Delta\nu/v_{\text{FSR}}$, with free-spectral range $\Delta\nu_{\text{FSR}} = c/(2L)$. As a result, the factor $1/2(kz_0)^2$ in Eq. (12) changes into a factor $1/(2\pi kR_m)$ in the equations for $\Delta\tilde{\nu} \approx \Delta\tilde{L}$ in Refs. [10,11]. Second, the $(N+1)^2$ contribution depends on the type of measurement. Equation (12) describes the change $\delta k_j = k_z - k < 0$ for a mode in an unfolded cavity, with fixed wave vector k and fixed geometry (L, R_m) . But in an actual experiment, one typically scans either the optical frequency or the cavity length to meet the resonance conditions for consecutive modes. A scan of the optical frequency will not affect the Rayleigh range $z_0 = k\gamma_0^2 = \sqrt{LR_m}$ and hence will go unnoticed in the final Eq. (12). This makes the required detuning to obtain resonance equal to $\Delta k = -\delta k_j$, if we neglect the frequency-dependent penetration depth of the commonly used Bragg mirrors [26]. But a scan of the cavity length will affect the Rayleigh range z_0 and the associated Gouy phase χ_0 , which in turn will introduce derivatives of $\chi(L_0 + \Delta L)$ and an additional $\propto (N+1)^2/(kz_0)^2$ term in the final equation for $\Delta L/L_0$, which then actually cancels the $\propto (N+1)^2/(kz_0)^2$ term in Eq. (12). Further discussion of the subtleties of the $(N+1)^2$ term is beyond the scope of this paper. We prefer to focus on the ℓ^2 and $\tilde{\ell}_s$ terms, which lift the frequency degeneracy of the modes within each N group and thereby introduce a spectral fine structure.

III. NONPARAXIAL FINE STRUCTURE FOR FIBERS

This section discusses the propagation of light in optical fibers with refractive-index profile $n = n(x, y)$ and compares the results with those obtained for short Fabry-Pérot cavities. The discussion is based on the general analysis from the book *Optical Waveguide Theory* by Snyder and Love [12]. It starts from the scalar wave equation for optical propagation in fibers:

$$(\Delta_\perp + k^2 n^2 - \beta^2)\Phi = 0, \quad (13)$$

where β is the propagation constant for the scalar electric field $E(\vec{r}) = \Phi(x, y)\exp(i\beta z)$. The solutions Φ_j of this equation are the transverse eigenmodes j of the fiber. The eigenvalues $\beta_j = \beta_0 + \delta\beta_j$ are the modal propagation constants, where $\beta_0 = kn_{\text{co}}$ serves as a reference and $\delta\beta_j < 0$ for the usual case with $n_{\text{co}} > n_{\text{cl}}$, where n_{co} and n_{cl} are the refractive indices of the core and cladding, respectively.

We consider fibers with rotation symmetry. The solutions of the scalar wave equation (13) for such fibers are traditionally called $\text{LP}_{\ell m}$ modes, with OAM quantum number $\tilde{\ell} = \pm\ell$ and radial quantum number $m = p + 1$. The eigenvalues of these modes typically depend on both ℓ and m . But for the parabolic fibers discussed below, the paraxial eigenvalues are partially degenerate as they depend on only the transverse order $N = 2(m - 1) + \ell$.

We are interested in fibers with an infinite parabolic refractive-index profile [12]

$$n^2(r) = n_{\text{co}}^2 \left[1 - 2\Delta \left(\frac{r}{\mathcal{R}} \right)^2 \right] \equiv n_{\text{co}}^2 \left(1 - \frac{r^2}{z_0^2} \right). \quad (14)$$

The first equation describes the parabolic profile in terms of its half width \mathcal{R} and its profile height parameter $\Delta = (n_{\text{co}}^2 - n_{\text{cl}}^2)/(2n_{\text{co}}^2)$ [12]. The second equation considers the limit $\mathcal{R} \rightarrow \infty$ and $\Delta \rightarrow \infty$ with fixed $z_0^2 \equiv \mathcal{R}^2/(2\Delta)$. Parabolic-index fibers are useful because they refocus the input light (a property also used in graded-index (GRIN) lenses) and because they have limited dispersion. Furthermore, they allow for analytic solutions and can hence serve as a convenient reference.

Next, we insert the index profile of Eq. (14) in the scalar wave equation (13). We introduce the dimensionless param-

ters $\tilde{r} \equiv r/\gamma_0$ and $\tilde{\Delta}_\perp \equiv \gamma_0^2 \Delta_\perp$, with $\gamma_0 = \sqrt{z_0/\beta_0}$, to obtain the dimensionless wave equation

$$[\tilde{\Delta}_\perp - \tilde{r}^2 + \gamma_0^2(\beta_0^2 - \beta^2)]\Phi = 0. \quad (15)$$

We thus recover the familiar equation for the (stationary modes of the) quantum harmonic oscillator and conclude that the eigenmodes of our fiber are the scalar LG modes. The eigenvalue equation $\gamma_0^2(\beta_0^2 - \beta^2) = 2(N+1)$ shows that these modes are equidistant in β^2 . A Taylor expansion of this equation yields

$$\beta_N = \beta_0 \sqrt{1 - \frac{2(N+1)}{\beta_0 z_0}} \approx \beta_0 - \frac{(N+1)}{z_0} - \frac{(N+1)^2}{2\beta_0 z_0^2}. \quad (16)$$

The first-order paraxial result $\beta_{\text{par}} = \beta_0 - (N+1)/z_0$ shows that any spatial profile, i.e., any superposition of modes, approximately repeats itself after propagation over a distance $\Delta z_{\text{period}} = 2\pi z_0$ in the fiber. The second-order correction $\delta\beta_{\text{scalar}} = -(N+1)^2/(2\beta_0 z_0^2)$ acts as a nonparaxial scalar correction on this propagation. This modest result agrees with the nonparaxial scalar correction for parabolic-index fibers determined by Petrov [13].

The transition from scalar to vector fields introduces a vector correction in the wave equation. In fibers, the vector correction originates from a $\vec{\nabla}(\vec{\nabla} \cdot \vec{E})$ term in Maxwell's equations. This term is absent in free space, where $\vec{\nabla} \cdot \vec{E} = 0$, but is present in fibers where $\vec{\nabla} \cdot (n^2 \vec{E}) = 0 \Rightarrow \vec{\nabla} \cdot \vec{E} = -\vec{E} \cdot \vec{\nabla} \ln[n^2(r)]$. In normalized units, the resulting vector wave equation is [12]

$$[\tilde{\Delta}_\perp - \tilde{r}^2 + \gamma_0^2(\beta_0^2 - \beta^2)]\tilde{\Phi}_\perp = -\tilde{\nabla}_\perp \{ \tilde{\Phi}_\perp \cdot \tilde{\nabla}_\perp \ln[n^2(r)] \} \\ = \frac{2}{\beta_0 z_0} \tilde{\nabla}_\perp (\tilde{\Phi}_\perp \cdot \tilde{r}_\perp). \quad (17)$$

The top equation describes the vector correction for any rotation-symmetric index profile. The bottom equation is valid only for fibers with the infinite parabolic profile of Eq. (14), where $\tilde{\nabla}_\perp \ln[n^2(r)] \approx -2\tilde{r}_\perp/z_0^2$ and $\tilde{\nabla}_\perp \ln[n^2(r)] \simeq -2\tilde{r}_\perp/(\beta_0 z_0)$ in normalized units. For comparison with the cavity results, we rewrite the bottom Eq. (17) as

$$\gamma_0^2(\beta_0^2 - \beta^2)\tilde{\Phi}_\perp = 2 \left(\tilde{\mathcal{H}}_{\text{par}} + \frac{1}{\beta_0 z_0} \tilde{\mathcal{H}}'_{\text{vec}} \right) \tilde{\Phi}_\perp, \quad (18)$$

where $\tilde{\mathcal{H}}_{\text{par}} = \frac{1}{2}(-\tilde{\Delta}_\perp + \tilde{r}^2)$ is the familiar paraxial operator and $\tilde{\mathcal{H}}'_{\text{vec}} = \tilde{\nabla}_\perp \otimes \tilde{r}_\perp$ is the vector correction in parabolic-index fibers. Using partial integration on bound modes, one can show that $\tilde{\mathcal{H}}'_{\text{vec}} = -\tilde{\mathcal{H}}_{\text{vec}}$, where $\tilde{\mathcal{H}}_{\text{vec}} = \tilde{r}_\perp \otimes \tilde{\nabla}_\perp$ is the spin-orbit operator in cavities.

Snyder and Love calculated the vector correction for fibers with an arbitrary circular index profile. Appendix C presents their general result in our notation and applies it to parabolic-index fibers to show that the resulting vector correction is

$$\langle \tilde{\Phi}_\perp | \tilde{\mathcal{H}}'_{\text{vec}} | \tilde{\Phi}_\perp \rangle = (1 + \tilde{\ell}s)/2 \quad (19)$$

for the complex vector modes in Eq. (10). We thus find that the vector correction in fibers also acts as a spin-orbit coupling, like in cavities, but that its sign is different as $\tilde{\mathcal{H}}'_{\text{vec}} = -\tilde{\mathcal{H}}_{\text{vec}}$ for parabolic-index fibers. As a result, the vector eigenmodes

are again the *A* and *B* modes with antialigned and aligned OAM and SAM, respectively. In fibers these modes are traditionally called EH (or TE or TM) and HE modes (see Table I).

By combining the above results, we obtain

$$\frac{\delta\beta_j}{\beta_0} = -\frac{N+1}{\beta_0 z_0} - \frac{1}{2(\beta_0 z_0)^2} [(N+1)^2 + (1 + \tilde{\ell}s)] \quad (20)$$

for the eigenmodes in parabolic-index fibers. This key result has the same functional form as the key (12) for short cavities if we associate $\beta_0 \leftrightarrow k$. The expansion parameter is also identical and is now given by $\alpha = 1/(\beta_0 z_0) = \Theta_0^2 = (\Theta_{\text{ext}}/n_{\text{co}})^2$, where Θ_{ext} is the opening angle of the fundamental mode outside the fiber and θ_0 is its internal angle (both radii are at $1/e$ of peak intensity). The paraxial contribution is identical in both equations, but the nonparaxial corrections differ (see below).

IV. COMPARISON CAVITY AND FIBER

This section compares the nonparaxial corrections in short cavities and parabolic-index fibers, as described by Eqs. (12) and (20). A quick look at these equations shows that (i) the $(N+1)^2$ terms in cavities and fibers have the same magnitude but opposite signs, (ii) the $f(N, \ell)$ term is absent in fibers, and (iii) the spin-orbit couplings in cavities and fibers also have the same magnitude but opposite signs. With regard to point (i), concerning the $(N+1)^2$ term, we note that the cavity effect originates from an expansion of the Gouy phase, while the fiber effect originates from a correction on the propagation constant. In relation to point (ii), the $f(N, \ell)$ term is absent in parabolic-index fibers since no analog exists for the propagation and wave-front correction that occur in cavities. An identical $f(N, \ell)$ term could be synthesized by modifying the fiber profile from $n^2(r) = n_{\text{co}}^2[1 - r^2/z_0^2]$ to $n^2(r) = n_{\text{co}}^2[1 - r^2/z_0^2 - c_4 r^4]$, with $c_4 = 3/(4z_0^4)$, but the physical interpretation thereof is yet unclear. Finally, with regard to point (iii), concerning the spin-orbit coupling, we note that its origin is again different in cavities and fibers. The spin-orbit coupling in cavities originates from the 56projection of a small longitudinal component of the field into an additional transverse component upon reflection from a curved mirror. The spin-orbit coupling in fibers, on the other hand, originates from a $\vec{\nabla}(\vec{\nabla} \cdot \vec{E})$ term in Maxwell's equation, which can be rewritten in a term that contains $\tilde{\nabla}_\perp \ln[n^2(r)]$.

As an aside, we note that the two forms of spin-orbit coupling encountered in the cavity and fiber system are part of the bigger picture of spin-orbit interactions of light, which involves any interaction of the photon spin with the spatial distribution of light [27,28]. The spin-orbit coupling considered in this paper is generated by the focusing of light, as quantified by the parameter $\alpha = \Theta_0^2 \ll 1$, and involves the longitudinal OAM of light. For beams with a tighter focus, the longitudinal field is stronger and also generates a sizable transverse OAM [29], but this is not yet important in our system.

Figure 2 visualizes the comparison between cavities and fibers in a way that summarizes the main message of this paper. The dashed vertical lines show how the modes cluster in groups with the same order N and how these paraxial groups are equally spaced by $-\delta k_z/k = 1/(kz_0) = \alpha \ll 1$ for cavities and by $-\delta\beta/\beta_0 = \alpha \ll 1$ for parabolic-index fibers. The 2×4 zoomed-in sections show how nonparaxial effects lift the degeneracy within each N group and thereby create

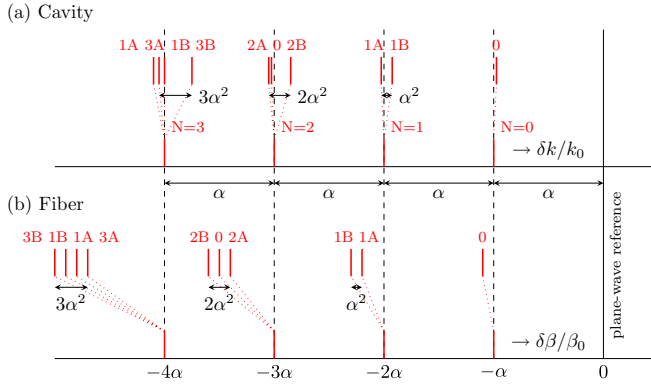


FIG. 2. Sketch of the modal spectrum for (a) the cavity and (b) fiber. The solid vertical line shows the plane-wave reference $k_z = k$ or $\beta = \beta_0$. The four dashed lines show the paraxial result for modes in the $N = 0, 1, 2, 3$ groups. The expanded views show the nonparaxial resonances relative to the paraxial values and the associated mode labels. See the text for further discussion.

a spectral fine structure [10,11]. These nonparaxial effects scale with α^2 , both in cavities and in fibers. But the ordering and exact resonance frequencies of the modes differ. The six arrows, for instance, show that the largest spin-orbit splitting within each N group is $N\alpha^2$ both for cavities and fibers but the signs are different. And while the resonance frequencies in fibers are regularly spaced at distances α^2 , the frequencies of the cavity modes are less regular due to the ℓ^2 term in Eq. (12).

The modes in Fig. 2 are labeled ℓA , ℓB , and 0, where ℓ is the absolute OAM quantum number and A or B indicates the OAM-SAM alignment of the $\ell \geq 1$ modes. Table I shows the intensity and polarization patterns of these modes. Table I also links these cavity-mode labels to the associated labels that are traditionally used in fiber technology. The associated fiber modes in Fig. 2 are (from left to right) $\{\text{HE}_{41}, \text{HE}_{22}, (\text{TM}_{02} \text{ and } \text{TE}_{02}), \text{EH}_{21}\}$ for the $N = 3$ group, $\{\text{HE}_{31}, \text{HE}_{12}, \text{EH}_{11}\}$ for the $N = 2$ group, $\{\text{HE}_{21}, (\text{TM}_{01} \text{ and } \text{TE}_{01})\}$ for the $N = 1$ group, and the fundamental HE_{11} for $N = 0$. Note that this ordering applies to only fibers with an infinite parabolic-index profile but is, for instance, different in step-index fibers [16,17]. The frequency degeneracy of $1A+$ and $1A-$ modes is then also typically lifted, but all modes still occur in pairs because of mirror symmetry.

For completeness, we note that the vector correction in circular fibers always acts as a spin-orbit coupling but that its magnitude depends on the index profile of the fiber (see Appendix C). In fibers with nonparabolic-index profiles, the spin-orbit coupling and the $\delta\beta$ splitting between the modes can be much stronger, making these modes more resilient against mode coupling. The first demonstrations of multimode transmission in fibers used four spatial modes [14,15], which were the fundamental ($N = 1$) HE_{11} mode and the ($N = 2$) TM_{01} , TE_{01} , and HE_{21} modes. More recent demonstrations have also used transverse modes from $N \geq 3$ groups: 24 modes in a specially designed fiber with an air core [18] and 15 modes in a trench-assisted graded-index fiber [19]. Using various types of mode multiplexing, the later system holds the current record with a communication bandwidth of more than 1 petabit/s in a multimode fiber [19].

V. SUMMARY AND OUTLOOK

In this paper, we discussed the nonparaxial fine structure in short rotational symmetric plano-concave Fabry-Pérot cavities and in fibers with rotation-symmetric cross sections. Corrections to the paraxial approximation were derived using perturbation theory with expansion parameters $\alpha = 1/(kz_0) = \Theta_0^2$ and $1/\beta_0 z_0$. These results were compared and discussed. The vector corrections to cavities and fibers were shown to result in spin-orbit couplings equal in magnitude but opposite in sign. The $(N + 1)^2$ -type scalar corrections that exist in both systems were also equal in magnitude but opposite in sign. Finally, the nonparaxial propagation and wave-front corrections predicted in cavities turned out to be absent in fibers and could be synthesized only by modifying their refractive-index profile. The resonance spectra, predicted on the basis of these nonparaxial corrections, is depicted in Fig. 2. The predictions for microcavities have been confirmed experimentally [11]. The fine structure in fibers is more difficult to interpret as the dominant paraxial term depends critically on the fiber's precise index profile in relation to the ideal infinite parabolic profile [16,17].

A crucial ingredient in this paper is the notion that the round-trip evolution of the optical field in a short cavity can be unfolded into a spread-out, coarse-grained evolution in one direction, where the reflections from the curved mirror create an effective waveguide. Although the key equations were derived for a plano-concave cavity, they are valid for any short cavity with mirrors with radii of curvatures R_1 and R_2 . In the short-cavity limit, $L \ll R_1, R_2$, one simply uses $1/z_0^2 = 1/(R_1 L) + 1/(R_2 L)$ instead of $1/z_0^2 = 1/(RL)$.

This paper analyzed rotation-symmetric cavities with ideal mirrors. We end by briefly considering three possible deformations beyond this ideal case. First, whether the mirrors have spherical or parabolic shapes is irrelevant in the considered short-cavity limit, but if the mirrors have very strong r^4 deformations, part of these deformations might still show up and slightly modify the $f(N, \ell)$ term in Eq. (12) [10,11], as L/R_m is never truly zero (see Ref. [11] for the observation of this modest effect). Second, if one uses Bragg mirrors instead of ideal mirrors, the polarization and angle dependence of these mirrors can introduce a frequency splitting between the $1A+$ and $1A-$ modes in each $1A$ pair through the Bragg effect [10,11]. In fibers with nonparabolic-index profiles, a related splitting exists between the TM and TE ($J = 0$, cylindrical vector) modes [16,17]. Finally, if one uses astigmatic mirrors instead of circular ones, this will introduce astigmatic terms of the form $x^2 - y^2$ in the evolution [10,11]. Further discussion of these effects is beyond this paper.

APPENDIX A: NONPARAXIAL SCALAR CORRECTIONS

This Appendix describes the physical origin of the three nonparaxial scalar corrections introduced in the main text and derives Eq. (7), which reads

$$\begin{aligned} \tilde{\mathcal{H}}_{\text{scalar}} &= \tilde{\mathcal{H}}_{\text{prop}} + \tilde{\mathcal{H}}_{\text{curv}} + \tilde{\mathcal{H}}_{\text{Gouy}} \\ &= \frac{1}{8} \left(\tilde{\Delta}_{\perp}^2 + 2\tilde{r}^4 - 4i\tilde{r}^2 \frac{\partial}{\partial \tilde{z}} \right). \end{aligned}$$

The propagation correction $\tilde{\mathcal{H}}_{\text{prop}}$ originates from the $\partial^2\psi/\partial z^2$ term in Eq. (1), or, equivalently, from the Taylor expansion of the longitudinal wave vector in Fourier space, $k_z = \sqrt{k^2 - k_\perp^2} \simeq k - k_\perp^2/(2k) - k_\perp^4/(8k^3)$ [5,10]. In real space, the nonparaxial $\delta k_z = -k_\perp^4/(8k^3)$ results in an operator $\tilde{\mathcal{H}}_{\text{prop}} = (kz_0^2) \times \Delta_\perp^2/(8k^3) = \frac{1}{8}\tilde{\Delta}_\perp^2$.

The wave-front correction $\tilde{\mathcal{H}}_{\text{wave}} = \tilde{\mathcal{H}}_{\text{curv}} + \tilde{\mathcal{H}}_{\text{Gouy}}$ describes the change upon reflection due to the mismatch between the incident wave front and the mirror shape [10]. For short cavities, $L \ll R_m$, this mismatch is typically dominated by the wave front of the eigenmodes

$$kz_{\text{wave}}(r, z) = \frac{kr^2}{2R(z)} - (N+1)\chi(z), \quad (\text{A1})$$

as these modes are typically compact enough not to notice the quartic component of the mirror shape $z_m(r) \approx r^2/2R_m + r^4/8R_m^3$ [10]. The wave front described by Eq. (A1) differs from the ideal form $kr^2/(2R_m) - (N+1)\chi(L)$ because both the curvature radius $R(z)$ and the phase lag $(N+1)\chi(z)$ vary slightly over the mirror surface $z = L - z_m \simeq L - r^2/(2R_m)$. A Taylor expansion of z_{wave} thus produces two corrections. The expansion of the $R(z)$ term results in a wave-front correction $\Delta z_{\text{wave}} = r^4/(4R_m^2L)$ and an associated operator $\tilde{\mathcal{H}}_{\text{curv}} = [kz_0^2/(2L)] \times 2k\Delta z_{\text{wave}} = \tilde{r}^4/4$. The expansion of $\chi(z)$ modifies the transformation from z to χ into $\chi(r, z) \simeq (z/z_0)[1 - r^2/(2LR_m)]$, such that $\partial/\partial\chi \simeq [1 + \tilde{r}^2/(2kz_0)]\partial/\partial\tilde{z}$, with $\tilde{z} \equiv z/z_0$. This results in an operator $\tilde{\mathcal{H}}_{\text{Gouy}} = -i\frac{\tilde{r}^2}{2}\frac{\partial}{\partial\tilde{z}}$. The combination of the three nonparaxial effects mentioned above results in the equation that we promised to derive.

APPENDIX B: NONPARAXIAL VECTOR CORRECTION

This Appendix shows that circularly polarized LG modes are eigenmodes of the vector operator and derives their eigenvalues. The main text introduces the circularly polarized LG mode as Eq. (10), where

$$\vec{\Phi}_\perp(r, \theta) = f(r)e^{i\tilde{\ell}\theta}\vec{e}_\pm = f(r)e^{i\tilde{J}\theta}(\vec{e}_r \pm i\vec{e}_\theta)/\sqrt{2},$$

and introduces the vector operator

$$\tilde{\mathcal{H}}_{\text{vec}} = \tilde{r}_\perp \otimes \tilde{\nabla}_\perp = -\frac{1}{2}(I_2 + \sigma_z \hat{\Sigma}_3), \quad \sigma_z = \begin{pmatrix} 1 & 0 \\ 0 & -1 \end{pmatrix}.$$

Application of $\tilde{\mathcal{H}}_{\text{vec}}$ to $\vec{\Phi}_\perp$ starts by splitting

$$\tilde{\nabla}_\perp \cdot \vec{\Phi}_\perp = \frac{1}{r} \frac{\partial(r\Phi_r)}{\partial r} + \frac{1}{r} \frac{\partial\Phi_\theta}{\partial\theta} \quad (\text{B1})$$

into contributions from the radial component Φ_r and the azimuthal components Φ_θ of the vector field $\vec{\Phi}_\perp$. Substitution of the above equation for $\vec{\Phi}_\perp$ in Eq. (B1) yields

$$r\tilde{\nabla}_\perp \cdot \vec{\Phi}_\perp = \left(\mp \tilde{J}f(r) + \frac{\partial[r f(r)]}{\partial r} \right) e^{i\tilde{J}\theta}/\sqrt{2} \quad (\text{B2})$$

and

$$\begin{aligned} \langle \vec{\Psi}_\perp | \tilde{\mathcal{H}}_{\text{vec}} | \vec{\Psi}_\perp \rangle &= \iint (\vec{r}_\perp \cdot \vec{\Psi}_\perp)^\dagger (\tilde{\nabla}_\perp \cdot \vec{\Psi}_\perp) r dr d\theta \\ &= \mp \tilde{J}/2 = -(1 + \tilde{\ell}s)/2, \end{aligned} \quad (\text{B3})$$

where the modes are assumed to be normalized and where the radial derivative is removed via partial integration. These are the eigenvalues that we promised to derive. The difference between $\vec{\Phi}_\perp$ and $\vec{\Psi}_\perp$ is a simple phase factor that disappears in the integration.

APPENDIX C: VECTOR CORRECTION IN FIBERS

Snyder and Love calculated the vector correction for fibers with an arbitrary rotation-symmetric index profile. Using perturbation theory, they found

$$\delta\beta^2 = - \iint \{ \tilde{\nabla}_\perp \ln[n^2(r)] \vec{\Psi}_\perp \}^\dagger (\tilde{\nabla}_\perp \cdot \vec{\Psi}_\perp) r dr d\theta, \quad (\text{C1})$$

where $\delta\beta^2 = \beta_{\text{vector}}^2 - \beta_{\text{par}}^2$ for bound normalized modes $\vec{\Psi}_\perp$. For fibers with an infinite parabolic-index profile $n^2(r) = n_{\text{co}}^2(1 - r^2/z_0^2)$, this integral is proportional to Eq. (B3), and

$$\delta\beta^2 = -\frac{(1 + \tilde{\ell}s)}{z_0^2} \Rightarrow \delta\beta_{\text{vector}} \approx -\frac{(1 + \tilde{\ell}s)}{2\beta_0 z_0^2}, \quad (\text{C2})$$

which is the vector correction in Eq. (20) in the main text.

For fibers with arbitrary rotation-symmetric index profiles, the conservation of OAM again allows one to write the eigenmodes as in Eq. (10) and split $\tilde{\nabla}_\perp \cdot \vec{\Psi}_\perp$ in a radial and azimuthal contribution as in Eq. (B1). Substitution in the general Eq. (C1) now yields

$$\delta\beta^2 \approx 2\beta_0\delta\beta = 2\beta_0(I_1 \mp I_2), \quad (\text{C3})$$

where the plus sign applies to all A modes with $\tilde{J} \neq 0$ and the minus sign applies to all B modes, including the $\ell = 0$ modes. The vector correction for the $\tilde{J} = 0$ modes are $\delta\beta = 0$ for the $1A-$ modes and $\delta\beta = 2(I_1 + I_2)$ for the $1A+$ modes [12]. Equation (C3) contains two integrals,

$$\begin{aligned} I_1 &= -\frac{1}{2} \int f(r) \frac{df(r)}{dr} \frac{d \ln[n^2(r)]}{dr} r dr, \\ I_2 &= -\frac{\ell}{2} \int \frac{1}{r} f^2(r) \frac{d \ln[n^2(r)]}{dr} r dr, \end{aligned}$$

which depend on $|\vec{\Psi}_\perp| = f(r)$ and $n(r)$. The same result can be found in Table 14.1 in *Optical Waveguide Theory* by Snyder and Love [12]. For typical fibers, $I_1 < 0$, and $I_2 > 0$. For infinite parabolic fibers $I_2 = -\ell I_1 = \ell/(2\beta_0 z_0^2)$. But the signs and magnitudes of I_1 and I_2 can be very different in fibers with more exotic index profiles, for instance, designed to enhance the spin-orbit coupling [15,17,18].

[1] D. Budker, S. M. Rochester, and V. V. Yashchuk, Obtaining frequency markers of variable separation with a spherical mirror Fabry-Perot interferometer, *Rev. Sci. Instrum.* **71**, 2984 (2000).

[2] R. N. Clarke and C. B. Rosenberg, Fabry-Perot and open resonators at microwave and millimetre wave frequencies, 2-300 GHz, *J. Phys. E* **15**, 9 (1982).

- [3] A. E. Siegman, *Lasers* (University Science Books, Mill Valley, California, 1988).
- [4] M. Lax, W. H. Louisell, and W. B. McKnight, From Maxwell to paraxial wave optics, *Phys. Rev. A* **11**, 1365 (1975).
- [5] C. W. Erickson, High order modes in a spherical Fabry-Perot resonator, *IEEE Trans. Microwave Theory Tech.* **23**, 218 (1975).
- [6] P. K. Yu and K.-M. Luk, High-order azimuthal modes in the open resonator, *Electron. Lett.* **19**, 539 (1983).
- [7] P. K. Yu and K.-M. Luk, Field patterns and resonant frequencies of high-order modes in an open resonator (short papers), *IEEE Trans. Microwave Theory Tech.* **32**, 641 (1984).
- [8] K.-M. Luk, Improvement in the resonant formula of a spherical Fabry-Perot resonator with unequal mirrors, *J. Opt. Soc. Am. A* **3**, 3 (1986).
- [9] M. Zeppenfeld and P. W. H. Pinkse, Calculating the fine structure of a Fabry-Perot resonator using spheroidal wave functions, *Opt. Express* **18**, 9580 (2010).
- [10] M. P. van Exter, M. Wubs, E. S. Hissink, and C. Koks, Fine structure in Fabry-Perot microcavity spectra, *Phys. Rev. A* **106**, 013501 (2022).
- [11] C. Koks, F. B. Baalbergen, and M. P. van Exter, Observation of microcavity fine structure, *Phys. Rev. A* **105**, 063502 (2022).
- [12] A. W. Snyder and J. D. Love, *Optical Waveguide Theory* (Springer Nature, Switzerland, 1983).
- [13] N. I. Petrov, Spin-orbit and tensor interactions of light in inhomogeneous isotropic media, *Phys. Rev. A* **88**, 023815 (2013).
- [14] N. Bozinovic, Y. Yue, Y. Ren, M. Tur, P. Kristensen, H. Huang, A. E. Willner, and S. Ramachandran, Terabit-scale orbital angular momentum mode division multiplexing in fibers, *Science* **340**, 1545 (2013).
- [15] B. Ung, P. Vaity, L. Wang, Y. Messaddeq, L. A. Rusch, and S. LaRochelle, Few-mode fiber with inverse-parabolic graded-index profile for transmission of OAM-carrying modes, *Opt. Express* **22**, 18044 (2014).
- [16] W. Zhang, K. Huang, L. Wei, P. Li, B. Jiang, D. Mao, F. Gao, T. Mei, G. Zhang, and J. Zhao, Cylindrical vector beam generation in fiber with mode selectivity and wavelength tunability over broadband by acoustic flexural wave, *Opt. Express* **24**, 16 (2016).
- [17] W. Qiao, T. Lei, Z. Wu, S. Gao, Z. Li, and X. Yuan, Approach to multiplexing fiber communication with cylindrical vector beams, *Opt. Lett.* **42**, 2579 (2017).
- [18] P. Gregg, P. Kristensen, A. Rubano, S. Golowich, L. Marrucci, and S. Ramachandran, Enhanced spin orbit interaction of light in highly confining optical fibers for mode division multiplexing, *Nat. Commun.* **10**, 4707 (2019).
- [19] G. Rademacher, B. J. Puttnam, R. S. Luis, T. A. Eriksson, N. K. Fontaine, M. Mazur, H. Chen, R. Ryf, D. T. Neilson, P. Sillard, F. Achten, Y. Awaji, and H. Furukawa, Peta-bit-per-second optical communications system using a standard cladding diameter 15-mode fiber, *Nat. Commun.* **12**, 4238 (2021).
- [20] G. Nienhuis, Operators in quantum optics, in *Structured Light for Optical Communication*, edited by M. D. Al-Amri, D. L. Andrews, and M. Babiker (Elsevier, Amsterdam, The Netherlands, 2021), pp. 107-137.
- [21] G. Nienhuis and L. Allen, Paraxial wave optics and harmonic oscillators, *Phys. Rev. A* **48**, 656 (1993).
- [22] G. Nienhuis and J. Visser, Angular momentum and vortices in paraxial beams, *J. Opt. A: Pure Appl. Opt.* **6**, S248 (2004).
- [23] G. R. Hadley, Effective index model for vertical-cavity surface-emitting lasers, *Opt. Lett.* **20**, 1483 (1995).
- [24] M. P. van Exter, E. S. Hissink, and C. Koks, From effective-index model to phase-plate model, *J. Opt.* **24**, 084001, (2021).
- [25] M. Uphoff, M. Brekenfeld, G. Rempe, and S. Ritter, Frequency splitting of polarization eigenmodes in microscopic Fabry-Perot cavities, *New J. Phys.* **17**, 013053 (2015).
- [26] C. Koks and M. P. van Exter, Microcavity resonance condition, quality factor, and mode volume are determined by different penetration depths, *Opt. Express* **29**, 6879 (2021).
- [27] F. Cardano and L. Marrucci, Spin-orbit photonics, *Nat. Photonics* **9**, 776 (2015).
- [28] K. Y. Bliokh, F. J. Rodríguez-Fortuño, F. Nori, and A. V. Zayats, Spin-orbit interactions of light, *Nat. Photonics* **9**, 796 (2015).
- [29] A. Aiello, P. Banzer, M. Neugebauer, and G. Leuchs, From transverse angular momentum to photonic wheels, *Nat. Photonics* **9**, 789 (2015).